

Hydrogen and aluminium in high-manganese twinning-induced plasticity steel

¹Do-Kyeong Han, ²Yongmin Kim, ²Heung Nam Han,

^{1,3}H.K.D.H. Bhadeshia and ¹Dong-Woo Suh

¹Graduate Institute of Ferrous Technology, POSTECH, Korea

²Department of Materials Science and Engineering and RIAM, Seoul National University,
Korea

³Materials Science and Metallurgy, University of Cambridge, UK

Abstract

Given that the penetration of hydrogen into austenite is confined to surface layers following prolonged hydrogen charging, experiments were devised using nanoindentation to assess the influence of hydrogen and aluminium on mechanical properties. It is found that the reduction in critical load for elastic to plastic transition in the hydrogen charged layers is smaller in the aluminium-alloyed steel, an effect that is not reflected in macroscopic tensile tests. The mechanism by which aluminium works to reduce hydrogen embrittlement is discussed.

Manganese-rich twinning-induced plasticity (TWIP) steels have an attractive combination of properties that are not generally matched by other advanced high strength steels [1-2]. Some of the focus has been on the variant containing 0.6 wt % C and 18~22 wt % Mn with other solutes to improve weldability and enhance the resistance to hydrogen embrittlement [3-5]. Aluminium is known to mitigate delayed fracture due to hydrogen but the underlying mechanism deserves further scrutiny. The suppression of martensite during deformation, a reduction in residual stress and the formation of Al oxide at the surface have been suggested in the context of aluminium additions, but clear evidence is lacking [6-8].

There is also a complication associated with the cathodic charging of tensile specimens [6-9]; the diffusion of hydrogen in austenite is extremely slow, some six orders of magnitude slower than in ferrite at room temperature [10]. Therefore, it is only the 50-100 μm surface region that is enriched with hydrogen after prolonged charging, making it difficult to assess the outcomes of typical tensile tests. The purpose of the present work was, therefore, to study the mechanical response of hydrogen charged TWIP steel using nanoindentation tests conducted directly on the enriched regions.

The steels investigated are Fe-0.6C-18Mn wt % alloys containing 0 (TW1) or 1.5 wt % Al (TW2), respectively. Cold-rolled sheets 1 mm in thickness were annealed at 900 °C for 15 min at ± 10 °C/s of heating and cooling rate. Metallographic samples were finish-polished with 0.25 μm diamond suspension, degreased with ethanol and characterized using a field-emission scanning electron microscopy and orientation imaging. For nanomechanical measurements, the metallographically prepared samples were electropolished and etched in a solution of 10 % perchloric acid and 90 % of ethanol at 13.0 V for 15 min.

Electrochemically charging was conducted in an aqueous solution of 3% sodium chloride

containing 0.3 g L^{-1} ammonium thiocyanate at a cathodic current density of 5 mA cm^{-2} for 48 h at a constant $25 \text{ }^\circ\text{C}$.

To analyse the total diffusible hydrogen content after cathodic charging, a conventional thermal desorption analysis was used at a constant heating rate of $100 \text{ }^\circ\text{C h}^{-1}$ to a maximum temperature of $300 \text{ }^\circ\text{C}$. Uniaxial tensile tests were conducted to assess the thickness of the embrittled layer via the fracture appearance. The crosshead speed was $0.03 \text{ mm}\cdot\text{s}^{-1}$, which corresponds to nominal strain rate of 10^{-3} s^{-1} .

Nanoindents were made using a TI750 machine; the load is applied at a constant $1000 \text{ }\mu\text{N s}^{-1}$ to maximum of $5000 \text{ }\mu\text{N}$. A Berkovich type diamond tip which has a centerline-to-face angle of 65.3° is used. Generally, the movement of indenter tip is controlled by displacement or loading rate. It is known that the displacement control would be more sensitive to the materials response [11-13]. In this research, however, loading rate control was adopted to measure precisely a strain burst pop-in during indentation [14,15]. To exclude the effects due to grain boundaries, such as the orientation of the indenter tip and boundary angle, after the indentation test, Figs. 1a,b were used to select indentations, excluding those that fell on grain boundaries [16-18]. The number of indentations is 49 (7×7 array) for the uncharged condition and 225 (15×15) for the charged condition. The actual number of selected points for analysis is 16 and 8 in TW1 and TW2 in the uncharged, and 25 and 40 in the charged condition respectively. Typical mechanical parameters were calculated as in [19]. The hardness is related to the maximum load, P_{max} and projected contact area, A as follows:

$$H = \frac{P_{\max}}{A} \quad (1)$$

where A is a function of h_c , which is depth of indenter contacting with the sample. The initial part of the load-displacement curve reflects Hertzian elastic behaviour [20]:

$$P = 1.33E_r R^{0.5} h^{1.5} \quad (2)$$

where E_r is the reduced elastic modulus, which considers effect of both the material and the indenter, R is the radius of the indenter tip curvature, and h is the indentation depth after the test.

Representative microstructures of the steels are shown in Fig. 1c,d. Orientation images revealed that both alloys are fully austenitic, with average grain sizes $9.5 \pm 1.8 \mu\text{m}$ and $10.5 \pm 3.0 \mu\text{m}$ in TW1 and TW2 respectively, i.e., no significant microstructural difference due to the aluminium addition. Fig. 2a,b show the thermal desorption curves of the hydrogen charged alloys and their macroscopic uniaxial tensile test curves with respect to the hydrogen charging. The total diffusible hydrogen was evaluated to be 0.30 and 0.42 ppmw in TW1 and TW2, respectively, consistent with previous work [21]. This does not of course account for the gradients that exist in the through thickness direction. Unlike other reports indicating the hydrogen embrittlement of TWIP steels [21,22], the present work finds an insignificant difference on due to hydrogen, given that the total elongation of conventional austenitic TWIP steel is reported to be around 60~70 % [21-24]. The reduced flow stress in the aluminium alloyed steel is as expected from previous work on uncharged samples [21]. Fig. 3 shows the fracture surface of hydrogen charged alloys. For both steels, the brittle part

of the fracture is localized to the surface layer with thickness about 15~20 μm . The remainder of the fracture surface is covered with ductile dimples, consistent with the fact that hydrogen does not diffuse rapidly in austenite [10]. Given that the thickness of brittle fractured layer in both TW1 and TW2 alloys are similar but the overall hydrogen content in TW2 alloy is high, it is presumed that the hydrogen concentration in surface layer of TW2 is greater than in TW1. The behaviour during tensile testing involves only a small fraction of hydrogen affected material, so the test is not sensitive to hydrogen charging.

Fig. 4a,b show the load-displacement curves TW1 and TW2 alloys depending on the hydrogen charging and Fig. 4 c,d are magnified plots of representative ones to clearly show the occurrence of 1st pop-in with the Hertzian elastic curves. The initial portion of loading is elastic, until the 1st pop-in is observed [20]. The derived mechanical parameters are summarized in Table 1. The Al addition decreases the hardness but has a negligible effect on the 1st pop-in load. Considering that the hardness is a measure of resistance to plastic flow and the 1st pop-in load is related to the transition from elastic to plastic behaviour, the changes suggest that the Al addition does not significantly change the yield strength but results in a reduction in the flow stress. It is known that in the absence of the aluminium addition, the TWIP steel exhibits a greater strain hardenability due to dynamic strain ageing and a greater tendency to twin during deformation as a consequence of a lower stacking fault energy [25].

The nanomechanical properties of hydrogen-charged alloys are significantly different from those of the uncharged ones as shown in Table 1. The hydrogen clearly leads to an increase in hardness of both alloys, consistent with previous reports on hydrogen in conventional austenitic stainless steels where the effect is explained by the enhancement of planar slip [26, 27]. The increase in TW1 and TW2 alloys is around 0.49 and 0.58 GPa, respectively. The

higher increase of hardness in TW2 is consistent with the greater quantity of hydrogen observed using the thermal desorption experiment.

It is interesting to consider the first pop-in, which indicates the initiation of plastic deformation shown in Fig 4c,d. After hydrogen is electrochemically charged into the steel, the average value of the 1st pop-in load shows a significant decrease in the investigated alloys. Average value of the pop-in load is decreased from 416 μN to 295 μN in TW1 and from 420 μN to 338 μN in TW2. The decrease in the load is 29.2 % and 19.5 %, respectively.

Such reductions have been investigated in many austenitic stainless steels [27-31]. Barnoush et al. [30] applied a classic dislocation theory to estimate the free energy for the homogeneous nucleation of a dislocation beneath the indentation tip, before and after hydrogen charging. It was concluded that dislocations could not be nucleated in the hydrogen charged condition at the measured pop-in load unless the elastic self-energy of a dislocation is decreased. Based on similar observations, Nibur et al. [27] suggest that the presence of hydrogen decreases the shear modulus, thereby leading to lowering the critical load for the dislocation nucleation. Since the decrease of shear modulus will reduce the elastic self-energy of dislocation, it can be regarded as intrinsic effect of hydrogen on materials property. Furthermore, the decrease of shear modulus will initiate dislocation gliding at a lower resolved shear stress on a primary slip plane, which is consistent with the hydrogen-enhanced local plasticity (HELP) mechanism often used to interpret hydrogen embrittlement [32]. In that respect, the smaller reduction in the 1st pop-in load in TW2 compared to TW1 in the presence of hydrogen is informative, given the greater hydrogen content recorded for the alloy. It might be concluded from this that aluminium negates some of the effect of hydrogen in leading to a reduction in the shear modulus, or in enhancing dislocation mobility in the context of the HELP mechanism. Of course, the underlying

mechanisms of the hydrogen embrittlement and delayed fracture are not necessarily the same. Nevertheless, the generation and propagation of cracks during fracture requires dislocation glide on the slip plane around the crack-tip [33], therefore, the suppression of local plasticity by decreasing dislocation mobility with aluminium addition is thought to contribute to the prevention of delayed fracture in high Mn TWIP steels.

Finally, we would like to point out the possibility of hydrogen effusion during the nanoindentation. In Fig. 4e, the hardness of hydrogen charged TW1 and TW2 alloys, which is collected for the analysis. The variation of hardness does not show any meaningful decrease, so it can be concluded that the results are not affected by the loss of hydrogen.

In summary, whereas conventional tensile testing of hydrogen charged specimens does not reveal changes in properties, because the hydrogen is only able to penetrate a thin surface layer of the tensile samples. On the other hand, nanoindentation of the hydrogen charged surfaces shows that the change in properties as indicated by the deviation from elasticity, is smaller in the aluminium-containing alloy. This could be interpreted in terms of published work if it is assumed that the effect of hydrogen in changing the shear modulus is reduced by the presence of aluminium.

Acknowledgement

YMK and HNH were supported by Basic Science Research Program through the NRF of Korea funded by the Ministry of Science, ICT and Future Planning (2013008806), and the NRF of Korea grant funded by the Korea government (MSIP) (No. 2008-0061900).

Table 1 Mechanical parameters calculated from the load-displacement curves.
 (Numbers in bracket represent standard deviation)

	Before hydrogen charging		After hydrogen charging	
	H (GPa)	Load at 1st pop-in (μN)	H (GPa)	Load at 1st pop-in (μN)
TW1	3.16 (0.10)	416 (93)	3.65 (0.09)	294 (56)
TW2	2.26 (0.11)	420 (99)	2.84 (0.08)	338 (76)

- [1] O. Grassel, L. Kruger, G. Frommeyer, and L.W. Meyer, *International Journal of Plasticity* 16 (2000) 1391
- [2] O. Bouaziz, S. Allain, and C. Scott, *Scripta Materialia* 58 (2008) 484
- [3] S. Kang, Y.S Jung, J.H Jun, and Y.K Lee, *Materials Science and Engineering A* 527 (2010) 745
- [4] J.E. Jin, and Y. K. Lee, *Materials Science and Engineering A* 527 (2009) 157
- [5] S. Allain, J.P. Chateau, and O. Bouaziz, *Materials Science and Engineering A* 387–389 (2004) 143
- [6] K.H. So, J.S. Kim, Y.S Chun, K.T. Park, Y.K. Lee, and C.S. Lee, *ISIJ International* 49 (2009) 1952
- [7] Y.S. Chun, K.T. Park and C.S. Lee, *Scripta Materialia* 66 (2012) 960
- [8] I.J. Park, K.H. Jeong, J.G. Jung, C.S. Lee, and Y.K. Lee, *International Journal of Hydrogen Energy* 37 (2012) 9925
- [9] J.A. Ronevich, S.K. Kim, J.G. Speer, and D.K. Matlock, *Scripta Materialia* 66 (2012) 956
- [10] Y. Sakamoto and H. Katayama, *Journal of the Japan Institute of Metals* 46 (1982) 805
- [11] W.A. Soer, J.Th.M. De Hosson, A.M. Minor, J.W. Morris Jr. and E.A. Stach, *Acta Materialia* 52 (2004) 5783
- [12] W.A. Soer, J.Th.M. De Hosson, A.M. Minor, Z. Shan, S.A. Syed Asif and O.L. Warren, *Applied Physics Letters* 90 (2007) 181924

- [13] J.Th.M. De Hosson, W.A. Soer, A.M. Minor, Z. Shan, E.A. Stach, S.A. Syed Asif and O.L. Warren, *Journal of Materials Science* 41 (2006) 7704
- [14] T.-H. Ahn, C.-S. Oh, D.H. Kim, K.H. Oh, H. Bei, E.P. George, H.N.Han, *Scripta Materialia* 63 (2010) 540
- [15] T.-H. Ahn, C.-S. Oh, K. Lee, E.P. George, H.N. Han, *Journal of Materials Research* 27 (2012) 39
- [16] W.A. Soer and J.Th.M. De Hosson, *Materials Letters* 59 (2005) 3192
- [17] E.T. Lilleodden and W.D. Nix, *Acta Materialia* 54 (2006) 1583
- [18] W.A. Soer, K.E. Aifantis, and J.Th.M. De Hosson, *Acta Materialia* 53 (2005) 4665
- [19] X. Li and B. Bhushan, *Materials Characterization*, 48 (2002), 11
- [20] K.L. Johnson, *Contact Mechanics, Normal contact of elastic solids - Hertz theory*, Cambridge University Press, Cambridge, England (1985) pp. 84-106.
- [21] J.H. Ryu, S.K. Kim, C.S. Lee, D.W. Suh, and H.K.D.H Bhadeshia, *Proceedings of the Royal Society A*, 469 (2013) 20120458
- [22] M. Koyama, E. Akiyama, T. Sawaguchi, D. Raabe, and K. Tsuzaki, *Scripta Materialia* 66 (2012) 459
- [23] O. Bouaziz, S. Allain, C.P. Scott, P. Cugy, and D. Barbier, *Current Opinion in Solid State and Material Science* 15 (2011) 141

- [24] M. Koyama, E. Akiyama, and K. Tsuzaki, *Scripta Materialia* 66 (2012) 947
- [25] K.T. Park, K.G. Jin, S.H. Han, S.W. Hwang, K. Choi, and C.S. Lee, *Materials Science and Engineering A* 527 (2010) 3651
- [26] D. G. Ulmer and C. J. Alstetter, *Acta Materialia* 39 (1991) 1237
- [27] K.A. Nibur, D.F. Bahr, and B.P. Somerday, *Acta Materialia* 54 (2006) 2677
- [28] M. Asgari, A. Barnoush, R. Johnsen, and R. Hoel, *Corrosion Science* 62 (2012) 51
- [29] Y. Yao, L.H. Qiao, and A.A. Volinsky, *Corrosion Science* 53 (2011) 2679
- [30] A. Barnoush, M. Asgari, and R. Johnsen, *Scripta Materialia* 66 (2012) 414
- [31] L. Zhang, B. An, S. Fukuyama, and K. Yokogawa, *Japanese Journal of Applied Physics* 48 (2009) 08JB08
- [32] H. K. Birnbaum, P. Sofronis, *Materials Science and Engineering A* 176 (1994) 191
- [33] S. P. Lynch, *Acta Metallurgica*, 36 (1988) 2639

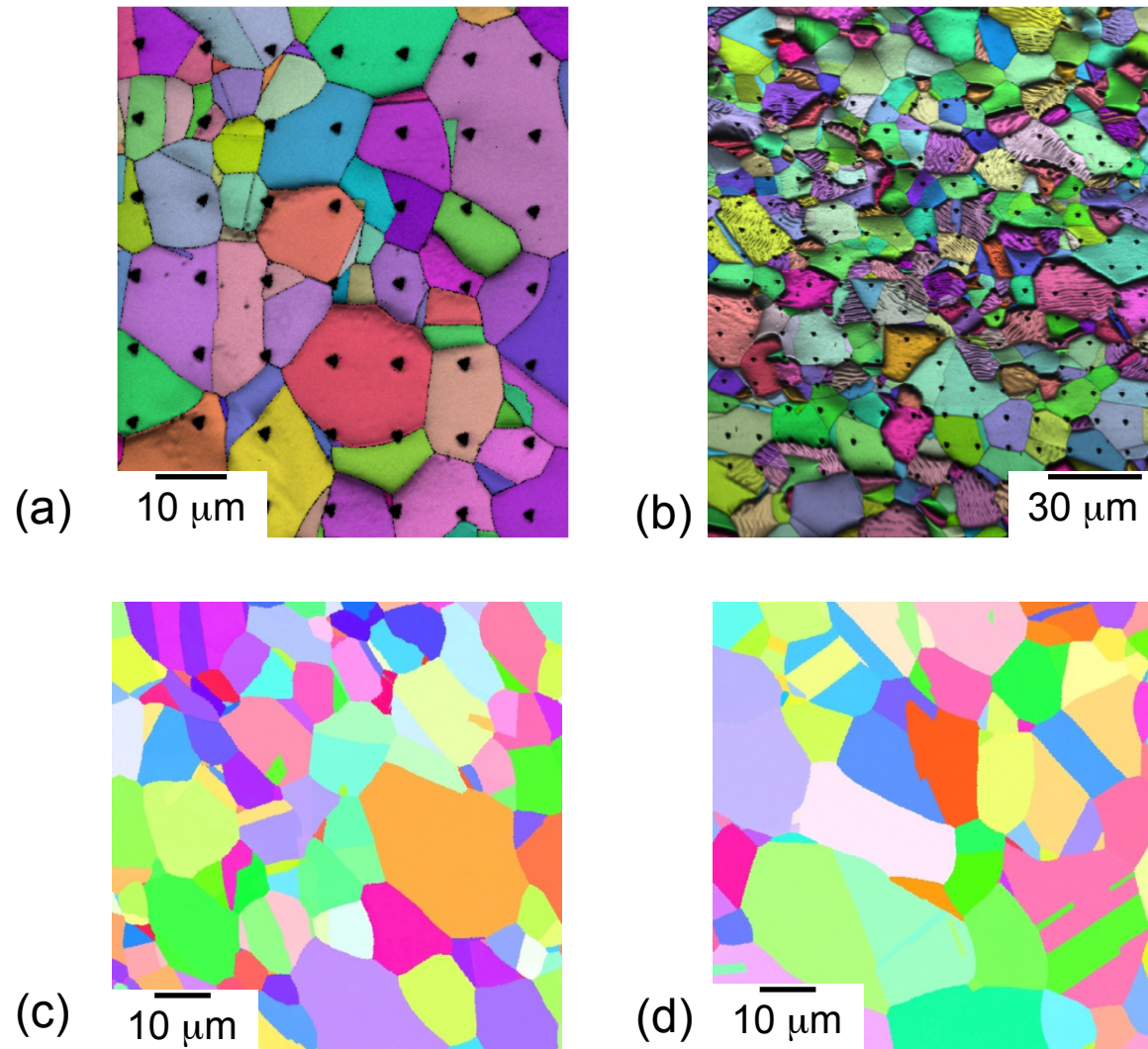
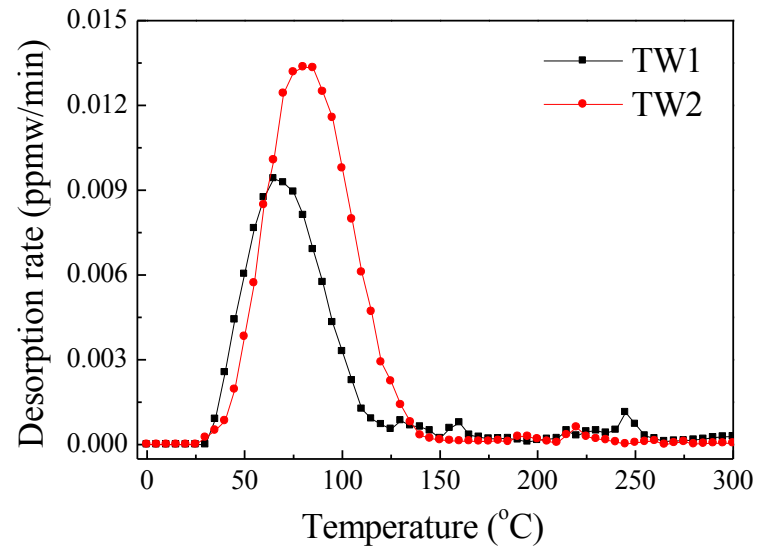
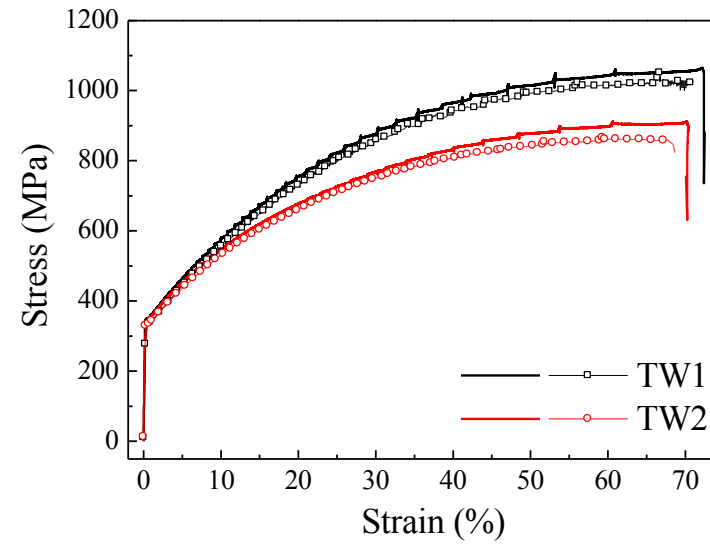


Figure 1. EBSD band contrast map of TW1 alloy after indenting (a) 7×7 arrays for hydrogen uncharged and (b) 15×15 arrays for hydrogen charged condition. Typical EBSD mapping of annealed (c) TW1 and (d) TW2 alloys.



(a)



(b)

Figure 2 (a) Thermal desorption profiles with hydrogen charging and (b) stress strain curves (symbols are uncharged and lines are charged ones)

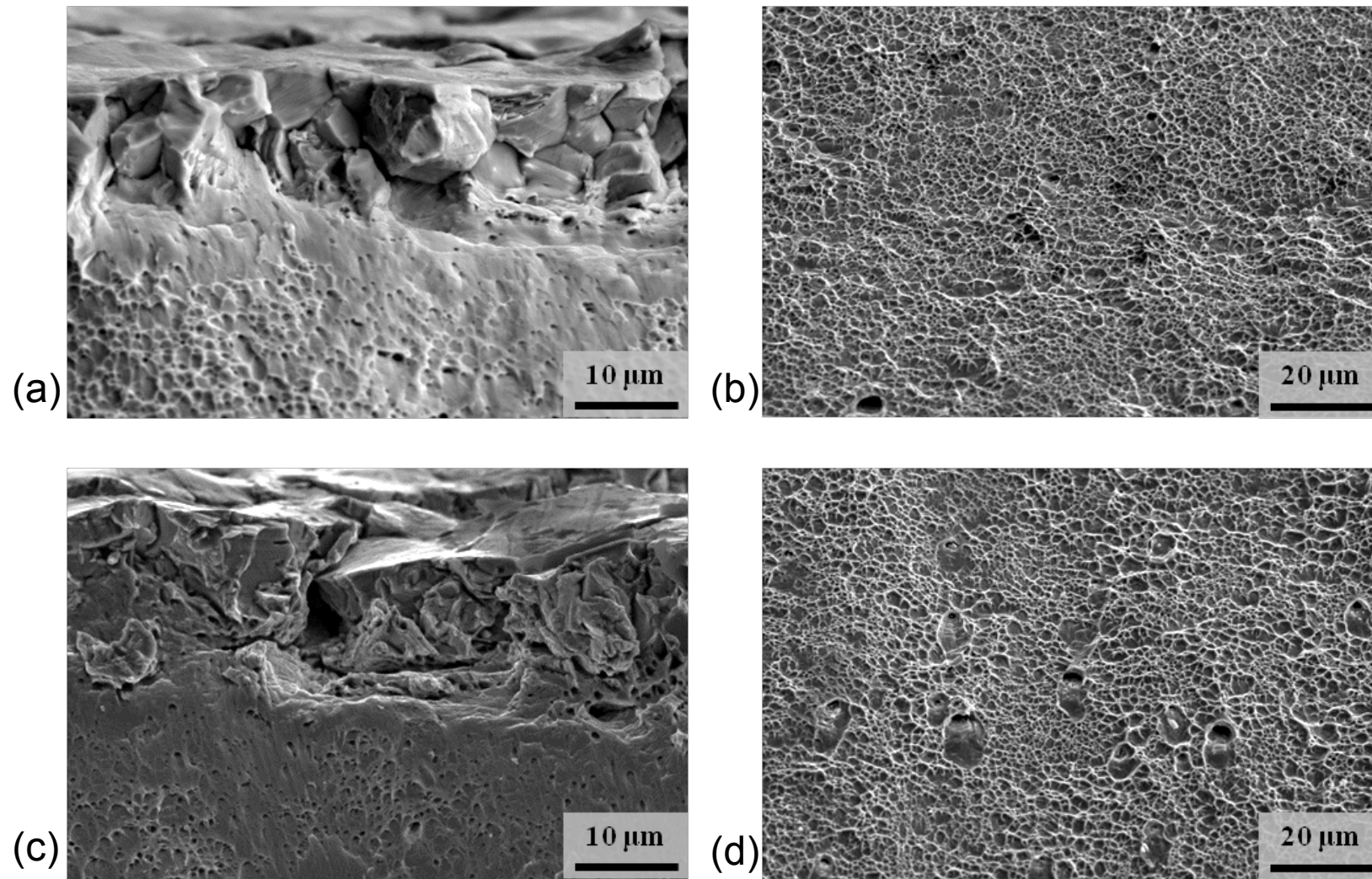
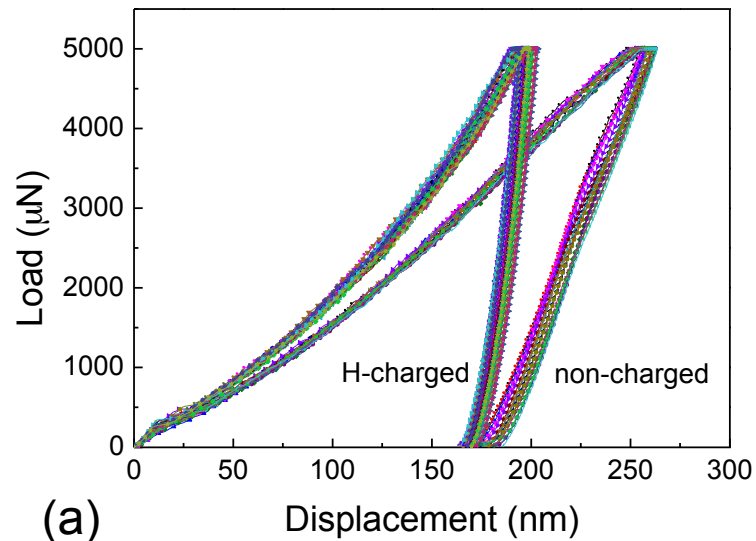
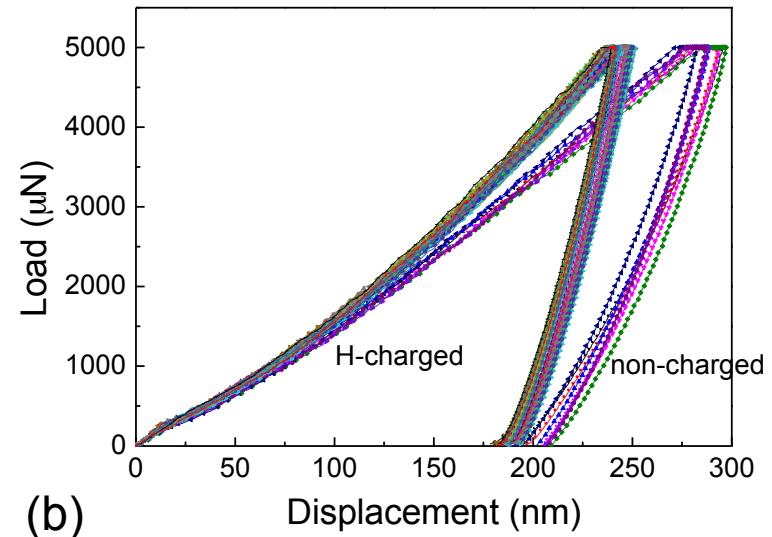


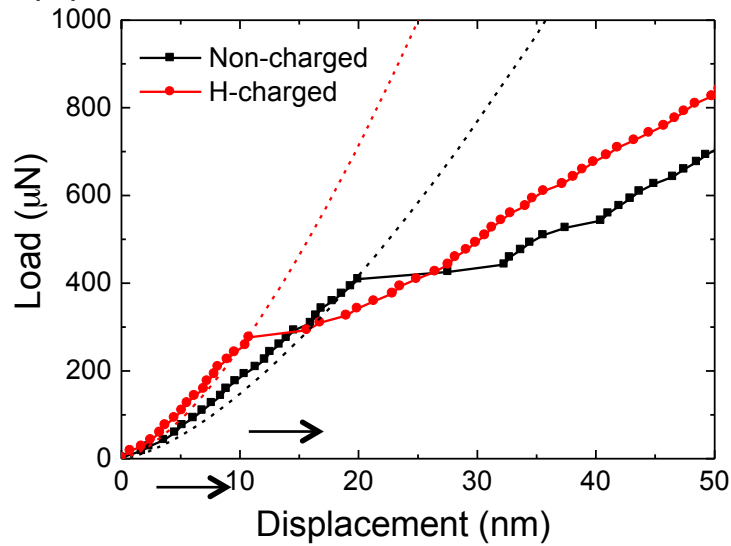
Figure 3 Fracture surfaces of the hydrogen charged (a,b) TW1 and (c,d) TW2 alloys after tensile test: (a), (c) represent fractography near the specimen surface. (b), (d) are magnified view of specimen centre.



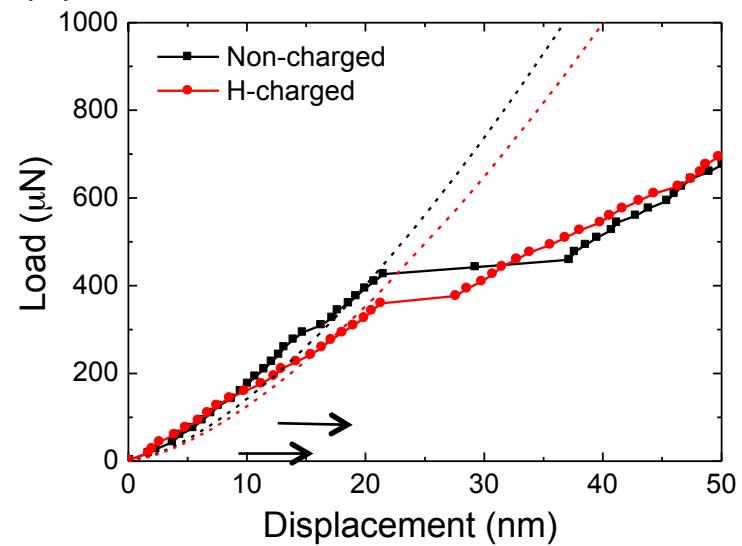
(a) Displacement (nm)



(b) Displacement (nm)

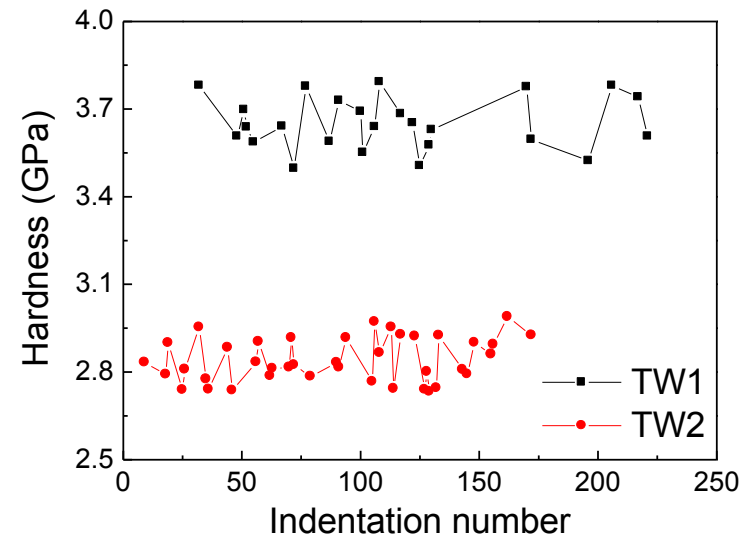


(c)



(d)

Figure 4 Nanomechanical load-displacement curves of (a) TW1, (b) TW2 depending on hydrogen charging. Magnified plots of representative load-displacement curves of (c) TW1 and (d) TW2, indicating the occurrence of 1st pop-in (arrows). (e) shows a variation of hardness in hydrogen charged TW1 and TW2 alloys as a progress of nanoindentation.



(e)